The Aeronautical Journal (2024), 1–19
doi:10.1017/aer.2024.65

ROYAL AERONAUTICAL SOCIETY

RESEARCH ARTICLE

Uncertainty quantification and sensitivity analysis of blade geometric deviation on compressor performance

T.Y. Ji[1], W.L. Chu[1] and Z.T. Guo[1]

School of Power and Energy, Northwestern Polytechnical University, Xi'an 710072, China
Corresponding author: W.L. Chu; Email: wlchu@nwpu.edu.cn

Received: 28 February 2024; **Revised:** 22 May 2024; **Accepted:** 4 June 2024

Keywords: machining deviation; compressor rotor; uncertainty quantification; aerodynamic performance; sensitivity analysis

Abstract

Carefully designing blade geometric parameters is necessary as they determine the aerodynamic performance of a rotor. However, manufacturing inaccuracies cause the blade geometric parameters to deviate randomly from the ideal design. Therefore, it is essential to quantify uncertainty and analyse the sensitivity of the blade geometric deviations on the compressor performance. This work considers a subsonic compressor rotor stage and examines samples with different geometry features using three-dimensional Reynolds-averaged Navier-Stokes simulations. A method to combine Halton sequence and non-intrusive polynomial chaos is adopted to perform the uncertainty quantitative (UQ) analysis. The Sobol' index and Spearman correlation coefficient help analyse the sensitivity and correlation between the compressor performance and blade geometric deviations, respectively. The results show that the fluctuation amplitude of the compressor performance decreases for lower mass flow rates, and the sensitivity of the compressor performance to the blade geometrical parameters varies with the working conditions. The effects of various blade geometric deviations on the compressor performance are independent and linearly superimposed, and the combined effects of different geometric deviations on the compressor performance are small.

Nomenclature

MCS	Monte Carlo simulation
PCA	principal component analysis
NIPC	non-intrusive polynomial chaos
CFD	computational fluid dynamics
UQ	uncertainty quantification
LE	leading edge
TE	trailing edge
Sim	numerical simulation results
Exp	experimental data
Sec.	sections from blade root to tip
SS	suction surface
PS	pressure surface

Symbols

m_a	mass flow rate
π	total pressure ratio
η	isentropic efficiency
ε_{Loo}	leave-one-out cross-validation error
S_i	first-order Sobol' index
S_i^T	total Sobol' index

$\delta(r)$	circumferential average total pressure loss coefficient
ρ	spearman correlation coefficient
ϕ	dissipation function

1.0 Introduction

Compressors are one of the most important components of aeroengines, so their aerodynamic performance and stability greatly influence the comprehensive performance of the engine [1, 2]. With continuous improvements in the compressor performance requirements of modern aeroengines, three-dimensional design structures of compressor rotor blades are becoming increasingly complex [3]. The increased degree of bending, twisting and sweeping of the blade increases the processing difficulty. However, geometric deviations inevitably exist on compressor blades and have strong uncertainty characteristics based on inherent machining vibrations and internal workpiece strain. Although deviations in various geometric parameters on the blade are relatively small, changes in the aerodynamic performance due to machining deviations are non-negligible [4]. As the basic working unit in the compressor, the rotor blade dictates the performance, and geometric variations between the manufactured blades and ideal designs significantly influence the aerodynamic performance of compressors and even complete engines [5]. Therefore, it is increasingly important to investigate the influence of blade geometric uncertainty on compressor performance and determine the critical geometric variables [6].

Bammert and Sandstede experimentally studied the impact of blade parameter deviations on the aerodynamic performance of a cascade and found that the cascade performance is greatly affected by blade thickness and stagger angle deviations but was less affected by blade chord length deviations [7]. Lange et al. captured three-dimensional measurements on a group of 150 blades and used Monte Carlo simulations (MCS) to quantify the effects of various blade profile machining deviations on the aerodynamic performance of high-pressure compressors [8–10]. They noticed that the isentropic efficiency and total pressure loss coefficient were most affected by thickness-related parameters. The blade stagger angle is the most important geometric parameter affecting the relative flow angle. Goodhand et al. experimentally and numerically studied the effects of blade leading shape deviations on the separation of the compressor rotor angular region [11, 12]. Cheng et al. investigated the influence of various rotor blade machining deviations on the compressor performance using orthogonal experiments [13]. The results indicated that compressor efficiency and flow rate changes are linear with the comprehensive effect of various machining deviations. Eric and Wang presented a computational framework for a simultaneous robust and tolerance design of compressor blades under manufacturing variability and evaluated the statistical performance of the compressor system via MCS [14]. David et al. studied the influence of machining deviations on compressor performance using the principal component analysis (PCA) based on actual measurement data from various blades [15, 16].

It is impossible to accurately study the influence of small geometric deviations experimentally due to limitations in the machining accuracy and processing costs. Therefore, most current research considers the influence of blade geometric deviations on compressor performance using numerical simulations [17]. The MCS method is the most straightforward approach to quantify uncertainty in parameter propagation, which readily provides the probability distribution of the response through random sampling. However, when dealing with multi-dimensional uncertainty problems, the MCS method requires significant random sampling to obtain accurate statistical results, significantly increasing the calculation time and requiring greater research costs [18]. The PCA method can greatly reduce the variable dimensions [19], which transforms geometric deviations into control point position deviations. However, these deviations cannot be used in machining processes to determine whether the measured blade is qualified. Thus, the output of the PCA cannot directly apply to machining processes.

In the past decade, the non-intrusive polynomial chaos (NIPC) method has been widely used in computational fluid dynamics (CFD) uncertainty analyses due to its ability to study the influence of different factors quantitatively [20–23]. The NIPC method generates samples based on the probability distribution of the variables and selects corresponding orthogonal polynomials to establish a mathematical model

Table 1. *Compressor design parameters*

Parameter	100% speed	71% speed
Design mass flow rate	5.6 kg/s	4.5kg/s
Inlet tip relative Mach number	0.78	0.7
Total pressure ratio	1.249	1.12
Adiabatic efficiency	0.905	0.92
Blade number	30	30
Rotation speed	15,200 r/min	10,765 r/min
Hub/tip ratio	0.61	0.61
Blade tip clearance	0.35 mm	0.35 mm

between the input and output variables. However, the number of samples required by the NIPC method increases exponentially with the dimensions of the input variable. This method also has the disadvantage of having too many samples when dealing with high-dimensional uncertainty problems. Therefore, a technique that combines the Halton sequence and NIPC is adopted to perform uncertainty quantitative (UQ) analysis. This approach not only retains the high efficiency of the NIPC method in dealing with uncertain problems but also solves the problem of having too many samples with high-dimensional data.

A subsonic compressor rotor stage was considered to quantify the uncertainty and analyse the sensitivity of the blade geometric deviations on the compressor performance. A total of 180 samples were uniformly generated using the Halton sequence based on the tolerance band of rotor blade geometric parameters specified in Refs. [24, 25]. The NIPC method quantified the uncertain impacts of deviations in the blade suction surface thickness, pressure surface thickness, leading-edge radius, trailing edge radius, chord length, stagger angle and tip clearance on the aerodynamic performance and stability of the compressor. Correlation and sensitivity analyses provide the geometric parameters that most influence compressor performance. The research conclusions provide reference value to the design and processing of compressor rotor blades.

2.0 Numerical methods

2.1 Research objective

This work utilised an isolated rotor from a single-stage, high-speed, axial compressor test rig, and the test facility is described in detail in Ref. [26]. Table 1 shows the relevant performance and design parameters of the rotor. Due to vibration of the test bench, experiments are rarely conducted at 100% design speed. A large number of experiments have been conducted at 71% design speed, and the detailed experimental data of the rotor at the 71% design speed are found in Ref. [27]. Therefore, this work chooses to investigate the impact of blade geometric deviations on the compressor performance at 71% design speed.

2.2 Numerical method verification

The computational domain grid was generated by the NUMECA/Autogrid5 module. The computational domain and the grid topology of the rotor are shown in Fig. 1, and the grid details are given in Table 2. In Fig. 1, LE and TE represent the leading edge and trailing edge of the blade, respectively. The rotor blade and Hub2 are rotating parts, while the rest are stationary. A single passage with periodic boundary conditions is used rather than full-annulus calculations to reduce the required computing resources. According to the conclusion of grid independence verification by Chi et al. [28] when the number of grids for the compressor rotor exceeds 0.97 million, the influence of grid density on the calculation results becomes negligible. Therefore, in this study, a grid number of 1.02 million is sufficient to ensure the accuracy of numerical calculation results.

Table 2. *Grid characteristics*

Property	Value
Grid structure	O-4H
Cells in radial direction	85
Cells in axial direction	177
Cells in tangential direction	53
Cell layers in the tip clearance	17
Total number of cells (millions)	1.02
Wall-normal size of the grid at the wall (m)	2×10^{-6}
y^+	<2

Table 3. *Calculation settings and boundary conditions*

Property	Value
Turbulent model	Spalart-Allmaras model
Time-discrete format	Second-order upwind difference format
Rotation speed	17,188 r/min
Initial total temperature	288 K
Initial total pressure	101,325 Pa
Initial airflow direction	Radial direction
Wall surface	Adiabatic and non-slip boundary

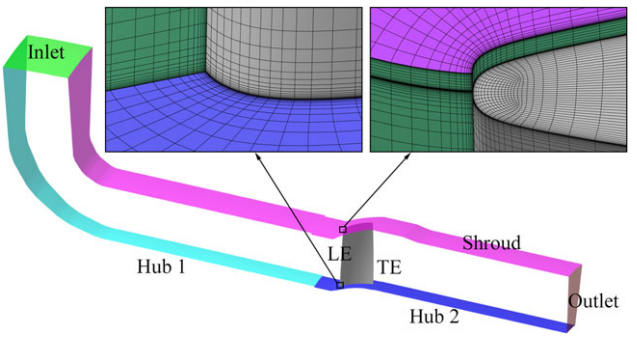

Figure 1. *Passage grid topology of the rotor.*

The commercial CFD solver NUMECA was used for the numerical simulations, and the flow field solution was obtained by calculating the three-dimensional Reynolds time-averaged Navier-Stokes equation. The calculation settings and boundary conditions of the numerical method are shown in Table 3. The computation is steady and compressible, and the multi-grid procedure is adopted to improve the convergence rate. In the stable working range of the compressor, the outlet interface provides the mass flow. The average static pressure at the outlet interface is enforced when approaching the near-stall boundary. The final numerical convergence point is regarded as the near-stall condition point after continuously increasing the static outlet pressure (ΔP=50 Pa) until a stable convergent solution is no longer obtained. The convergence criterion of the numerical calculations is that the mass flow rate (m_a), isentropic efficiency (η), and total pressure ratio (π) remain constant and the global residual is less than 10^{-6}.

Figure 2 compares the compressor performance curves between the numerical simulations and experimental data under the 71% design speed (10,765 r/min). The subscripts Sim and Exp represent the numerical simulation results and experimental data, respectively. The total pressure ratio performance curve obtained from the numerical calculations agrees well with the experimental data, with a maximum

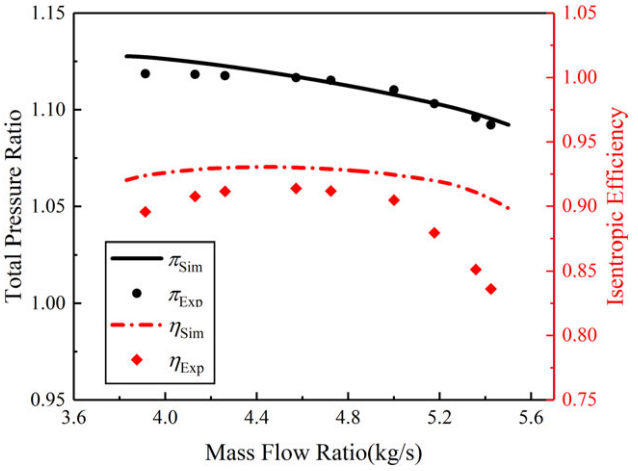

Figure 2. *Compressor rotor characteristics.*

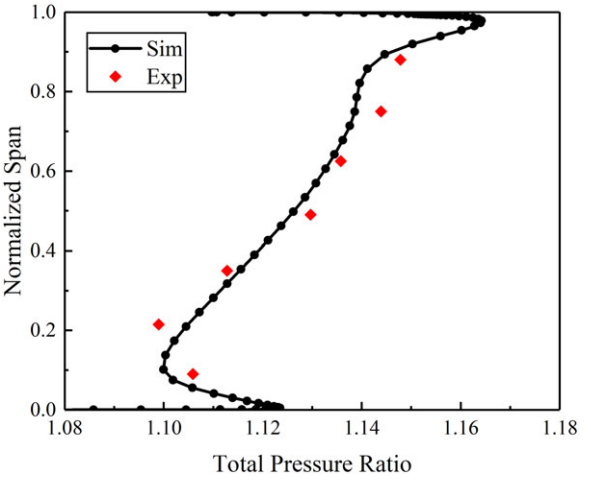

Figure 3. *Spanwise distribution of the total pressure ratio at the near-stall condition.*

relative error of 0.78%. In contrast, the numerical results of the isentropic efficiency performance are slightly larger than the experimental data, but the two have the same trend with the flow rate. The average relative error is less than 3%, which is consistent with the numerical simulation results by other researchers [29]. Further, the relative error between the blocked mass flow obtained by the numerical calculations and the experimental data is less than 1.4%, and the relative error of the near-stall mass flow is less than 2.1%. The lower efficiency from the experimental data may be due to partial energy dissipation caused by the inability to achieve adiabatic conditions and the significant influence of temperature measurements on the efficiency of the low-pressure specific compressor. Furthermore, limitations in the accuracy of turbulence models used in numerical simulations can also contribute to discrepancies between experimental data and numerical simulations.

Figure 3 compares the circumferential average total pressure ratio distributed along the radial direction between the numerical simulations and experimental data at the near-stall condition. The numerical simulations agree well with the experimental data, with the best agreement in the mid-leaf region. The numerical calculations also simulate a "C" shape distribution of the total pressure ratio in the blade root

area. The trend of the total pressure ratio along the radial direction is consistent with the experimental data.

Although there are errors between the numerical results and the experiment data, the numerical approach provides credible predictions. The benchmark in the comparative study is the numerical results rather than the experimental data. The minor calculation errors in the numerical results can be eliminated in the comparative analysis due to the consistency of the benchmark [30]. Therefore, the numerical method is used in the following research.

3.0 Uncertainty quantification method

3.1 Non-intrusive polynomial chaos

Due to randomness in the geometric deviations during machining [31], it is important to quantify the associated uncertainty in the compressor performance. The NIPC approach is used as the UQ method due to its high efficiency in dealing with uncertainty problems [32]. The NIPC method estimates the characteristics of random output variables based on deterministic solutions from specific samples. The NIPC method performs a series expansion on the random variables using orthogonal polynomials and uses the polynomial coefficients to reflect the random characteristics of output variables as:

$$F(\theta) = c_0\Psi_0 + \sum_{i_1=1}^{\infty} c_{i_1}\Psi_1(\xi_{i_1}(\theta)) + \sum_{i_1=1}^{\infty}\sum_{i_2=1}^{i_1} c_{i_1 i_2}\Psi_2(\xi_{i_1}(\theta), \xi_{i_2}(\theta)) + \ldots \tag{1}$$

where $\xi(\theta)$ represents the input random variable and Ψrepresents the orthogonal polynomial basis. The above equation can be abbreviated to the standard format:

$$F(\xi) = \sum_{j=0}^{P} \hat{c}_j\Psi_j(\xi) \tag{2}$$

When the rth-order NIPC method is used to handle m-dimensional uncertainty problems, the upper limit of the summation P is calculated as:

$$P = \frac{(m+r)!}{m!r!} - 1 \tag{3}$$

After obtaining the output response $F(\xi)$ and orthonormal basis response $\Psi_i(\xi)$ of each sample, the following matrix form is constructed:

$$\begin{bmatrix} \Psi_0(\xi_0) & \cdots & \Psi_P(\xi_0) \\ \vdots & \ddots & \vdots \\ \Psi_0(\xi_n) & \cdots & \Psi_P(\xi_n) \end{bmatrix} \begin{bmatrix} \hat{c}_0 \\ \vdots \\ \hat{c}_P \end{bmatrix} = \begin{bmatrix} F(\xi_0) \\ \vdots \\ F(\xi_n) \end{bmatrix} \tag{4}$$

This can be written in vector form as:

$$\Psi c = F \tag{5}$$

Then, the polynomial coefficients can be obtained by the least square method as:

$$c = (\Psi^T\Psi)^{-1}\Psi^T F \tag{6}$$

Based on the orthogonality of the chaotic polynomial, the mean (μ) and variance (σ^2) of the random output variable $F(\xi)$ can be obtained by:

$$\mu = \hat{c}_0 \tag{7}$$

$$\sigma^2 = \sum_{j=1}^{P} \left[\hat{c}_j^2 \left\langle \Psi_j^2 \right\rangle\right] \tag{8}$$

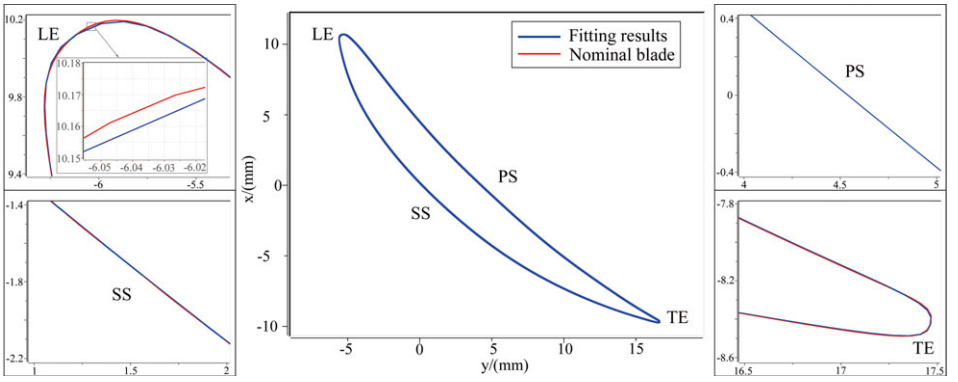

Figure 4. *Fitting effect of the Sec. 3 profile.*

3.2 Sample point selection

The traditional rth-order NIPC method obtains the sample points by solving the $(r+1)$-order polynomial. Thus, for the one-dimensional uncertainty problem, the number of sample points required for the rth-order NIPC method is $(r+1)$. When dealing with m-dimensional uncertainty problems, the number of sample points of the rth-order NIPC method increases to $(r+1)^m$. The number of sample points is far more than the number of polynomial chaos expansion coefficients, which results in unnecessary simulations. Therefore, the traditional method of obtaining sample points is unsuitable for the NIPC method when dealing with high-dimensional uncertainty problems.

In this work, a 180×7 matrix is generated by the Halton sequence, with 180 sample points and seven types of geometric deviations. These deviations include the blade suction surface thickness deviation (STD), pressure surface thickness deviation (PTD), leading-edge radius deviation (LRD), trailing-edge radius deviation (TRD), chord length deviation (CLD), stagger angle deviation (SAD) and tip clearance deviation (TCD). The Halton sequence is a set of pseudo-random sequences whose sample points are fixed and evenly distributed in space, which effectively avoids the phenomenon of "sample overlap" and "space hole". Further increasing the number of sample points on a Halton sequence only encrypts the original sample space without forming the "clustering phenomenon" of the sample points. The corresponding geometric deviations of each sample can be obtained from the constructed 180x7 matrix. Finally, a total of 180 blade samples are developed after reconstructing the blade model, described as follows.

4.0 Blade model reconstruction method

4.1 Parameterisation of the rotor blade model

The rotor blade geometry model is first parameterised to study the influence of geometric uncertainty on the combustor performance. This work uses the NUMECA/Autoblade module to realise rotor parameterisation. Six spanwise sections at 0.0, 0.2, 0.4, 0.6, 0.8 and 1.0 are parameterised from the root to the tip, which are denoted as Sec. 1 to Sec. 6. The Bezier curves are selected to fit the profile of each section. The section outlines are decomposed into their camber and thickness distributions. The fitting results and the nominal blade section of Sec. 3 are compared in Fig. 4 as an example, and the local square figures are enlarged 25 times. The comparison results in Fig. 4 indicate that the fitting results are almost entirely coincident with the suction surface (SS) and pressure surface (PS) of the section, and the fitting errors at the leading edge (LE) and trailing edge (TE) do not exceed 0.005 mm. Errors from curve fitting the geometric deviations of the blade are relatively small. Thus, the parameterisation of the blade model can accurately obtain the geometric parameters of the rotor. Therein, the blade samples with geometric deviations are reconstructed based on the parameterisation results.

Table 4. *Blade parameter tolerance band*

Geometric deviation type	Deviation range	Probability distribution	Blade parameter	Relative deviation range
Leading edge radius deviation (LRD)	[−0.10 mm, 0.10 mm]	$N(0, 0.0333^2)$	0.72 mm	[−13.89%, 13.89%]
Trailing edge radius deviation (TRD)	[−0.06 mm, 0.06 mm]	$N(0, 0.02^2)$	0.12 mm	[−50%, 50%]
Suction surface thickness deviation (STD)	[−0.13 mm, 0.13 mm]	$N(0, 0.0433^2)$	2.01 mm	[−6.47%, 6.47%]
Pressure surface thickness deviation (PTD)	[−0.13 mm, 0.13 mm]	$N(0, 0.0433^2)$	2.01 mm	[−6.47%, 6.47%]
Chord length deviation (CLD)	[−0.52 mm, 0.52 mm]	$N(0, 0.1733^2)$	30 mm	[−1.73%, 1.73%]
Tip clearance deviation (TCD)	[−0.025 mm, 0.025 mm]	$N(0, 0.00833^2)$	0.3 mm	[−8.33%, 8.33%]
Stagger angle deviation (SAD)	[−0.5°, 0.5°]	$N(0, 0.1678^2)$	29°	[−1.72%, 1.72%]

4.2 Geometric deviation and probability distribution

Based on the relevant content in Refs. [24] and [25]. Table 4 gives the maximum deviation range of the blade geometry, and the corresponding probability distribution of each geometric deviation is assumed. When the total number of workpieces is sufficiently large, the geometric deviation distribution based on the Gaussian process agrees well with the machining deviation measurement data [33]. Therefore, the blade geometric deviations are considered a Gaussian distribution, and the standard deviation of the probability distribution is determined from the 3σ criterion. Based on the parameterisation of the rotor, the blade model with geometry deviation is reconstructed by changing the value of each geometric parameter on the six sections. The geometric deviation distributions on each section are considered the same to simplify the model reconstruction process and save computing resources.

4.3 Blade samples

The corresponding geometric deviations of each sample are obtained from the 180x7 matrix generated by the Halton sequence. Changing the geometric parameters of the blade provides samples with different geometric deviations. Taking Sec. 3 as an example, the blade profiles of the 180 samples are shown in Fig. 5 and are compared with the nominal blade. The local square figures are enlarged by 25 times. The grid number and structure are the same for all samples, and the numerical methods are the same. The influence of blade geometric deviations on the compressor performance is analysed using the numerical simulations of the 180 samples and the uncertainty quantification of the calculation results. In order to reduce the mesh discretisation error between different blade samples during numerical calculations, the mesh structure and computational setting of each blade sample are the same as the nominal blade.

5.0 Results analysis

5.1 Accuracy verification of UQ method

The NIPC method is a response surface method. When using it for UQ analyses, one must first determine its order and verify the response accuracy. First, the total pressure ratio of the 180 samples at a mass

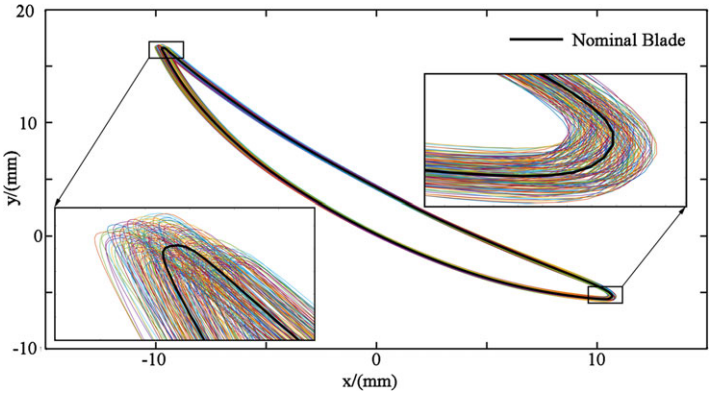

Figure 5. *Profile of the Sec. 3 samples compared with the nominal blade.*

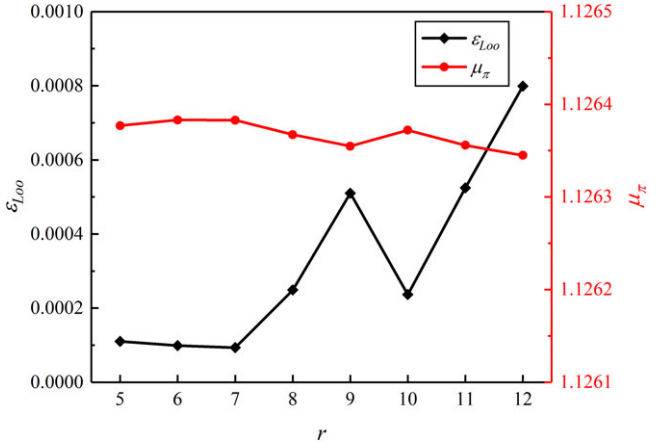

Figure 6. *Comparison of the UQ results for different orders of the NIPC method.*

flow rate of 4 kg/s is calculated, and the NIPC response models with different orders are constructed. In Fig. 6, the mean values of the total pressure ratios calculated from different orders are compared. The leave-one-out cross-validation error (ε_{Loo}) is introduced to quantify the response accuracy of each NIPC model. The ε_{Loo} is given by [34]:

$$\varepsilon_{Loo} = \frac{\sum_{i=1}^{N} \left(\frac{M(\xi_i) - M_{NIPC}(\xi_i)}{1 - h_i} \right)^2}{\sum_{i=1}^{N} (M(\xi_i) - \mu)^2} \tag{9}$$

where $M(\xi_i)$ is the real functional value at the ith sample point, $M_{NIPC}(\xi_i)$ is the response value of the NIPC model at the ith sample point, N is the total number of samples, μ is the mean from Equation (7), and h_i is the ith component of the vector given by:

$$h = diag\left(\Psi(\Psi^T\Psi)^{-1}\Psi^T\right) \tag{10}$$

The Ψ is the experimental matrix in Eq. (4). The $\varepsilon_{Loo}$is evaluated from previously performed numerical experiments; that is, no additional model evaluation is required. A comparative study indicates that this technique performs well regarding estimation bias and mean-square error [35].

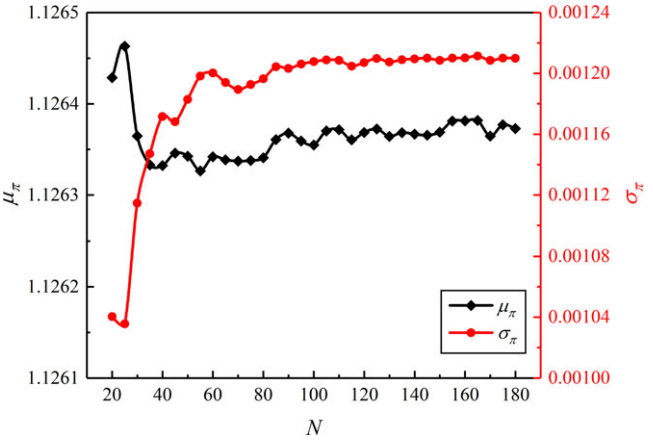

Figure 7. *Quantitative results of the NIPC method for different numbers of samples.*

As seen from Fig. 6, the mean value of the total pressure ratio, as quantified by NIPC methods with different orders, fluctuates over a small range. Thus, the calculation accuracy of the compressor performance statistical parameters from the 5th to 12th-order NIPC method do not differ much. However, when the NIPC method with an order less than 7 is used, the value of ε_{Loo} gradually decreases as the order increases, indicating that the accuracy of the NIPC model increases. When the NIPC method has an order greater than 7, the value of ε_{Loo} is significantly larger, meaning that the higher-order NIPC methods have overfitting problems. Therein, the fitting error of the space edge region increases and the accuracy of the NIPC model decreases. Therefore, the 7th-order NIPC method is used to conduct the UQ analyses for the influence of the blade geometric deviations on the compressor performance.

Figure 7 quantifies the results of the mean and standard deviation of the total pressure ratio as a function of the number of samples using the 7th-order NIPC method. As the number of samples increases, the statistical result of the total pressure ratio gradually converges, indicating that the 180 samples used in this work are sufficient to ensure that the NIPC method has sufficient convergence. In addition, 20 blade samples are randomly constructed within the tolerance band as the test group. The NIPC model built using the 180 samples predicts the total pressure ratio of the test group samples. Figure 8 compares the response values with the results from the numerical simulations. The abscissa is the response value of the NIPC model, and the ordinate is the numerical simulation results. The response values of the NIPC model are nearly identical to the numerical simulation results. Therefore, the 7th-order NIPC response model constructed using 180 samples has sufficient accuracy for the UQ analyses.

5.2 Performance curve variation

The UQ analyses of the compressor performance at six mass flow rates (5.46, 5.15, 4.84, 4.53, 4.22 and 3.91 kg/s) are performed, denoted as OP1-OP6. The OP1 condition is close to the plugging point of the nominal blade, the OP4 condition is close to the peak efficiency and the OP6 condition is close to the near-stall point. The mean value of the compressor performance at each condition is shown in Fig. 9, and the standard deviation is marked with error bars. The mean performance is also compared with the performance curve of the nominal blade in Fig. 9.

The comparison between the mean and nominal blade performance curves shows that the blade geometric deviation leads to an average compressor performance that is lower than the design performance parameter. However, differences between the mean and design performances are relatively small and only obvious in the OP1 condition, which has the largest mass flow rate. Comparing the distributions of the compressor performance standard deviation under different conditions indicates that the fluctuation

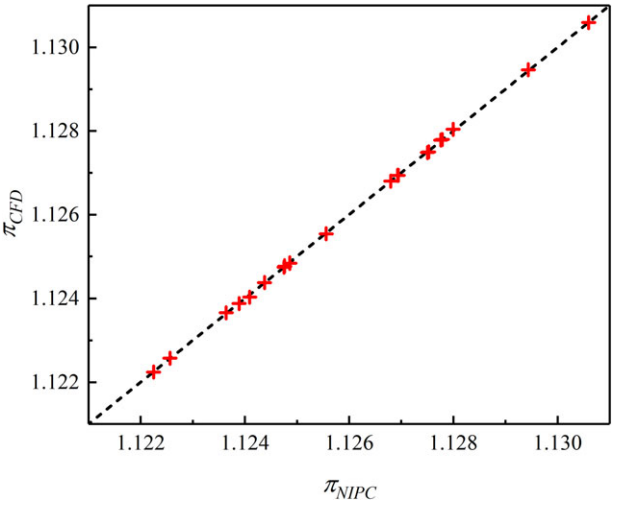

Figure 8. *Comparison of the NIPC model predictions and numerical simulations.*

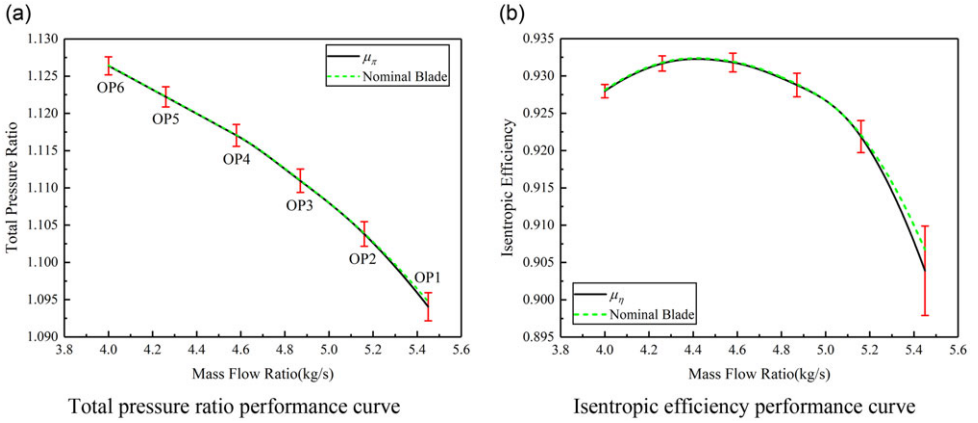

Figure 9. *UQ results of the performance curves.*

amplitude of the total pressure ratio and isentropic efficiency decreases for lower mass flow rates. The isentropic efficiency standard deviation decreases faster than the total pressure ratio standard deviation under the same conditions. This indicates that the sensitivity of the isentropic efficiency to blade geometric deviations increases significantly with the mass flow rate. In contrast, the mass flow rate minimises the sensitivity of the total pressure ratio on the blade geometric deviations.

5.3 Sensitivity and correlation analyses

The Sobol' index and Spearman correlation coefficient are used to analyse the sensitivity and correlation between the compressor performance and blade geometric deviation, respectively. The Sobol' sensitivity analysis method is a global approach introduced by Sobol [36]. The core idea is to decompose the objective function $f(\boldsymbol{x})$ into a combination of single- and multi-parameter functions and use the ratio of the variance for the corresponding function value of each input to the total variance of the model as the sensitivity evaluation standard of the corresponding input. The firstst-order and higher-order sensitivity coefficients corresponding to each input are calculated using the ratio of variance [37]. The index with

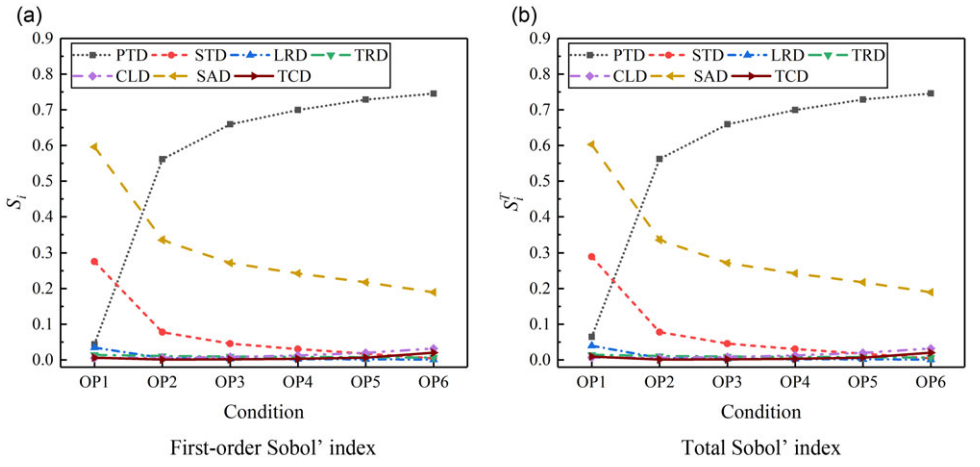

Figure 10. *Sobol' index for the total pressure ratio under different conditions.*

respect to one input variable x_i is called the first-order Sobol' index and represents the effect of x_i alone, which is denoted S_i. The total Sobol' index of input variable x_i, denoted S_i^T, is the sum of all Sobol' indices involving this variable. The calculation process of S_i and S_i^T is described in detail in Ref. [38].

The Spearman rank correlation coefficient (ρ) refers to a nonparametric index that measures the dependence of two variables [39]. It evaluates the correlation between two statistical variables using a monotone equation:

$$\rho = 1 - \frac{6\sum_{i=1}^{n}(x_i - y_i)^2}{n(n^2-1)} \tag{11}$$

where n is the size of the variable dataset, and x_i and y_i represent the ranks of the ith element in the variable datasets $\boldsymbol{x}$ and $\boldsymbol{y}$, respectively. The closer ρ is to 0, the smaller the monotonic correlation is between the two variables. When ρ is 1 or -1, the two variables are entirely monotonic and positively or negatively correlated.

A total of 10^5 samples are selected as the statistical group within the tolerance band based on the geometric deviation probability distribution The corresponding response values of each sample are obtained from the constructed NIPC response model. The calculated S_i and ${S_i}^T$ for the compressor total pressure ratio and isentropic efficiency under the six operating conditions are shown in Figs. 10 and 11. Comparing Figs. 10(a) and (b) shows that differences between S_i and ${S_i}^T$ for the same geometric deviation are relatively small under the same working conditions. This indicates that the effects of various blade geometric deviations on the compressor total pressure ratio are independent and linearly superimposed. The combined effects of different geometric deviations on the total pressure ratio are small.

The Sobol' index for various geometric deviations in different conditions suggests that in the OP1 condition, the total pressure ratio of the compressor has the greatest sensitivity to the SAD and STD with minimal sensitivity to the other geometric deviations. As the state approaches near-stall, the sensitivities of the compressor total pressure ratio to the PTD gradually increase. The influence of the PTD on the total pressure ratio is the largest in OP2. At the same time, the sensitivities of the compressor total pressure ratio to the SAD and the STD gradually decrease. In OP4, the sensitivity of the total pressure ratio to the STD becomes relatively small. The sensitivities of the total pressure ratio to the LRD, TRD, CLD and TCD are relatively low under all conditions.

Figure 11 shows that the influences of various blade geometrical deviations on the compressor isentropic efficiency can be considered as independent and linearly superimposed. The blade STD has the

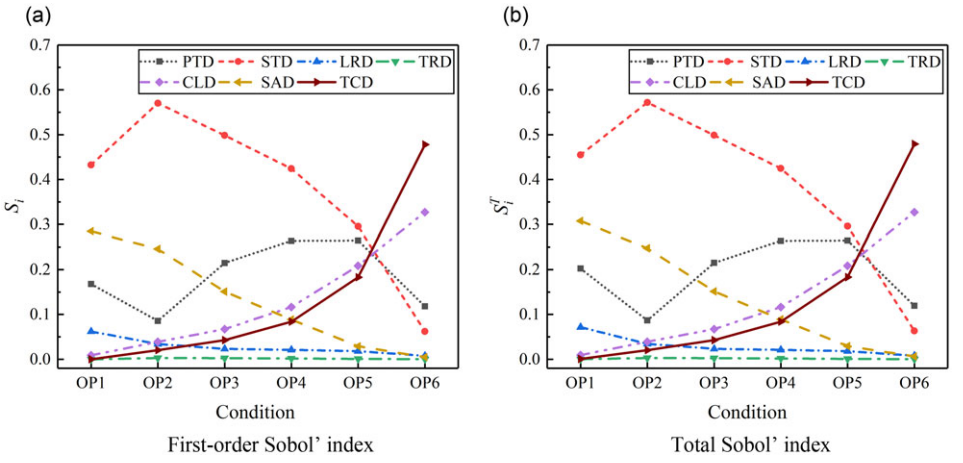

Figure 11. *Sobol' index for the isentropic efficiency under different conditions.*

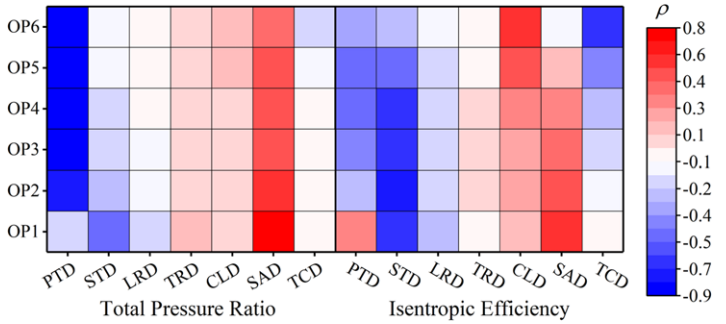

Figure 12. *Correlations between the compressor performance and blade geometric deviations under different conditions.*

greatest influence on the compressor isentropic efficiency under the OP1-OP5 conditions, and the isentropic efficiency is most sensitive to the TCD in the OP6 condition. The trend of the Sobol' index for various geometric deviations in different conditions indicates that the sensitivities of the compressor isentropic efficiency to the STD and SAD gradually decrease as the state approaches near-stall. The sensitivities of the isentropic efficiency to both STD and SAD become very small in the OP6 condition. The sensitivities of the compressor isentropic efficiency to the CLD and the TCD gradually increase, and their influence on the isentropic efficiency is the greatest in OP6. The Sobol' index of the PTD fluctuates over a wide range and always significantly affects the isentropic efficiency. The sensitivities of the isentropic efficiency to the LRD and TRD are relatively low in all conditions.

Figure 12 shows the Spearman correlation coefficient between the compressor performance and blade geometric deviation under the six conditions. The figure compares the influence of various geometric deviations on the compressor performance while showing the associated correlations. The compressor total pressure ratio has strong monotone correlations with the PTD in the OP1-OP6 conditions and the SAD in the OP1-OP5 conditions. This indicates a stronger influence of these two geometric deviations. There are strong monotonic correlations between the compressor isentropic efficiency and the STD in the OP1-OP4 conditions, SAD in the OP1-OP3 conditions, CLD in the OP5-OP6 conditions and TCD in the OP5-OP6 conditions. Thus, these geometric deviations have greater effects on the isentropic efficiency in the corresponding conditions.

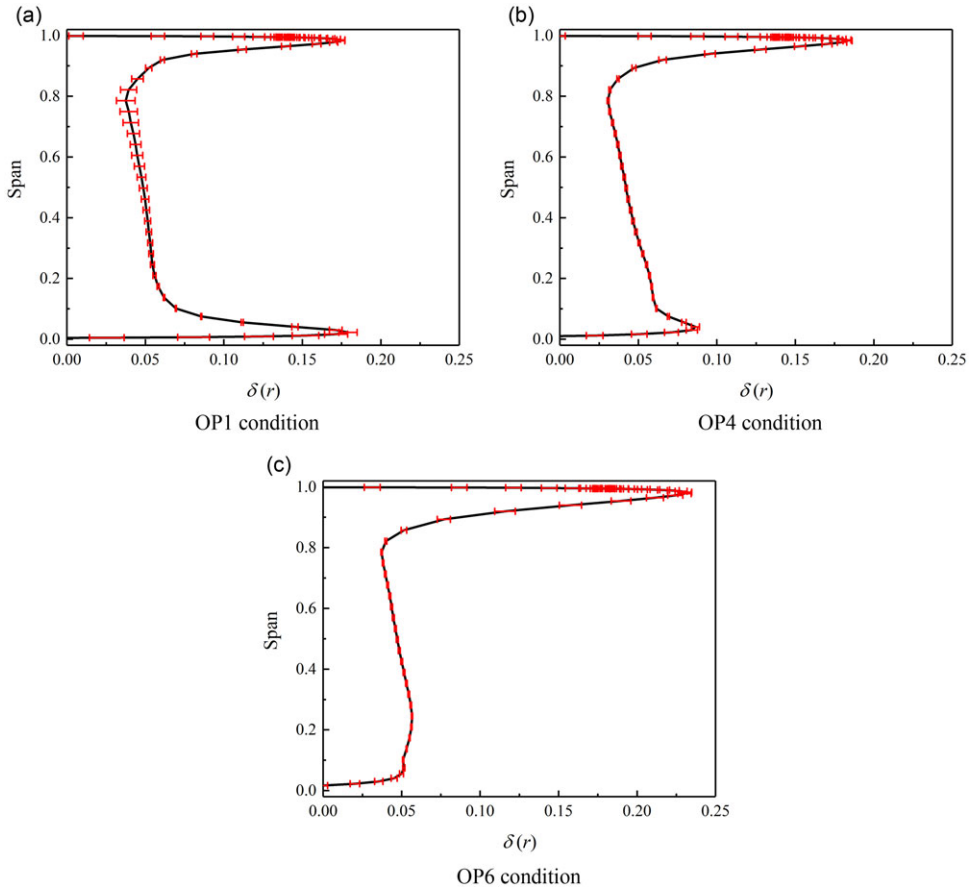

Figure 13. *Spanwise distribution of $\delta(r)$ and its standard deviation.*

Figure 12 shows that the PTD and the STD are significantly negatively correlated with the compressor total pressure ratio and isentropic efficiency under most conditions. The SAD is significantly positively correlated with the compressor performance in most conditions. Therefore, the machining accuracy of the blade geometric parameters should be ensured as much as possible. Suppose the machining accuracy cannot be improved. In this case, the tolerance range of the blade thickness and stagger angle can be adjusted appropriately to ensure the regular use of the compressor by sacrificing other design parameters and guaranteeing that the design parameters with higher priorities meet the requirements.

5.4 Analysis of the influence of flow field structure

The circumferential average total pressure loss coefficient ($\delta(r)$) characterises the radial distribution of the flow loss as:

$$\delta(r) = \frac{p_t(r)_{1,avg} - p_t(r)_{2,avg}}{p_t(r)_{1,avg} - p(r)_{1,avg}} \tag{12}$$

where p_t is the relative total pressure, and p is the static pressure. The subscript *avg* represents the circumferential average, and 1 and 2 represent plane 1 and plane 2, respectively. Figure 13 shows the spanwise distribution of $\delta(r)$ in the OP1, OP4, and OP6 conditions. The standard deviations of $\delta(r)$ at different spans are marked with error bars.

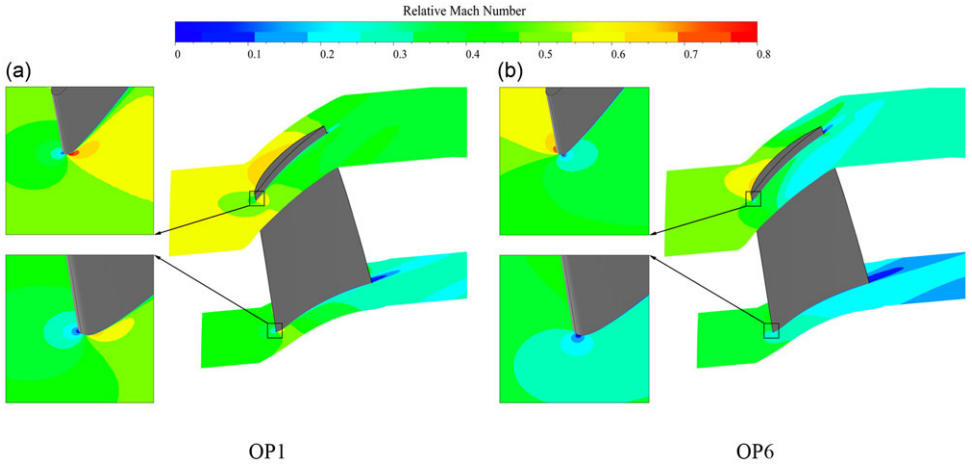

Figure 14. *Relative Mach number distribution at the 5% span and 95% span.*

Figure 13(a) indicates large flow losses in both the blade root and tip regions in OP1. In OP4, the flow loss in the blade root region is significantly reduced, and the flow loss change in the blade tip region is weak. Therefore, the compressor isentropic efficiency in OP4 is greater than that in OP1. In OP6, although the flow loss in the blade root region is further reduced, flow loss in the blade tip region is significantly increased. So, the compressor isentropic efficiency in OP6 is less than that in OP4.

The fluctuation amplitude of $\delta(r)$ in different working conditions indicates that the flow loss in the range of the 0–5% span and 40–90% span in OP1 fluctuates significantly. In OP4, fluctuations in the flow loss in the 40–80% span range become marginal, and the fluctuation amplitudes of flow in the root region are lower than those in OP1. Therefore, in Fig. 13(b), the fluctuation amplitude of the compressor isentropic efficiency in OP4 is significantly smaller than in OP1. Compared with OP4, the fluctuation amplitude of flow loss in the blade root region is reduced considerably in OP6, but the fluctuation amplitude of the flow loss in the 90–95% span range increases. Therefore, fluctuations of the compressor isentropic efficiency in OP6 are slightly weaker than in OP4.

The relative Mach number distributions of the 5% span and 95% span of the nominal blade are given in Fig. 14. There is a point at the leading edge where the relative Mach number is 0; that is, the airflow is stagnant. The airflow is divided into two parts at the stagnation point: toward the blade pressure surface and suction surface. The airflow attack angle is negative (positive) if the stagnation point is biased towards the suction (pressure) surface. In OP1, both the root and tip regions have negative attack angles. In OP6, the airflow in the tip region changes to a positive attack angle, and the airflow attack angle in the root region is nearly 0. Figure 15 compares the streamline distributions near the 5% span leading edge of the nominal blade in OP1 and OP6, and changes in the airflow attack angle are more intuitive.

Figures 16 and 17 show the distributions of the relative Mach number standard deviation at the 5% span and 95% span in OP1, OP4 and OP6. The figures analyse the flow field regions that are significantly affected by blade geometric deviations. It is noted that blade geometric deviations cause the absolute position of the grid nodes for each sample to change, but the grid structure of each sample is the same. Thus, the relative position of each grid node relative to the blade surface remains the same. After calculating the relative Mach number standard deviation on each grid node, the calculation results are combined with the grid nodes of the nominal blade.

Figure 16 shows that in the OP1 condition, the attack angle of the airflow in the blade root region is negative, which results in large flow field fluctuations near the pressure surface side of the leading edge (region 1). Then, the flow field fluctuations on the blade pressure surface side gradually spread to

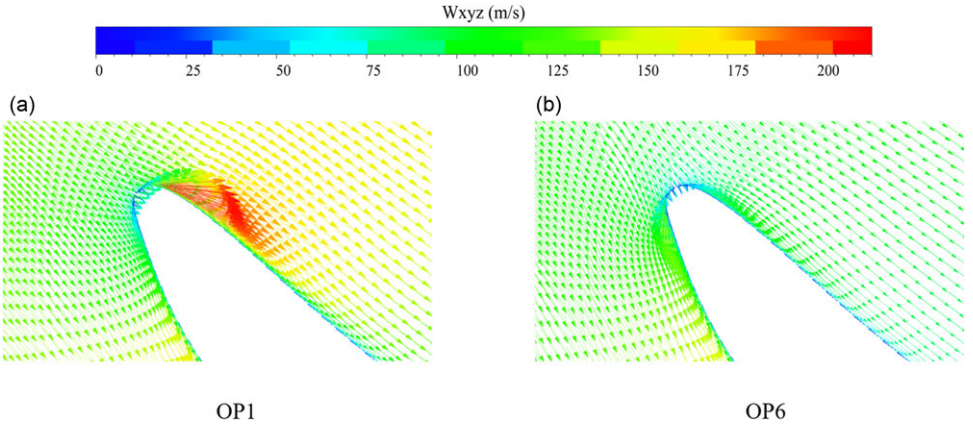

Figure 15. *Variations in airflow attack angle near the leading edge at the 5% span.*

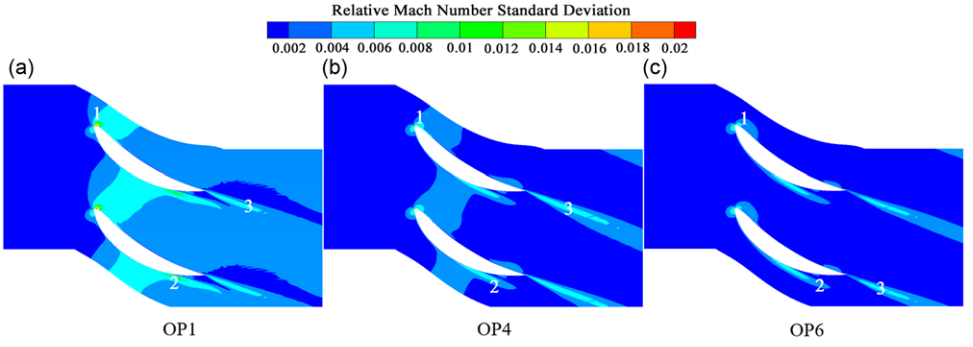

Figure 16. *Distributions of the relative Mach number standard deviation at the 5% span.*

the suction surface, causing flow field fluctuations over the entire blade passage. The absolute value of the negative attack angle in the blade root region is smaller in OP4 than in OP1. Therefore, in OP4, the fluctuation amplitude of the flow field in region 1 decreases, which further reduces the amplitude and range of fluctuations over the entire blade passage and leads to fluctuations in the flow loss of the blade root region to be smaller than OP1. In OP6, the attack angle in the blade root region is nearly 0, and the strong flow field fluctuations only exist near the leading edge (region 1), suction surface boundary layer (region 2) and wake area (region 3). Therefore, the fluctuation amplitude of the flow loss in the blade root region is the smallest in OP6.

Figure 17 indicates that in OP1, the airflow attack angle in the blade tip region is negative, and the flow field fluctuations in region 1 are relatively strong. In addition, a region with significant flow field fluctuations appears in the middle and downstream of the blade passage (region 4), which corresponds to the low-speed area created by the tip clearance leakage flow. In OP4, the airflow attack angle in the blade tip region is nearly 0. The flow field fluctuation amplitude in region 1 of OP4 decreases relative to OP1, but the fluctuation amplitude of the flow field in region 4 increases, and its influence range extends to the upstream of the blade passage. In OP6, the airflow attack angle in the tip region is positive, the flow field fluctuations in region 1 are further weakened, and the flow field fluctuations in region 2 are more robust. At the same time, the influence range of region 4 increases, and the fluctuations of the flow field are enhanced. This indicates that the tip clearance leakage flow is more sensitive to blade geometric deviations at small mass flow rates. Therefore, the fluctuation amplitude of the flow loss in the blade tip region is the largest in OP6.

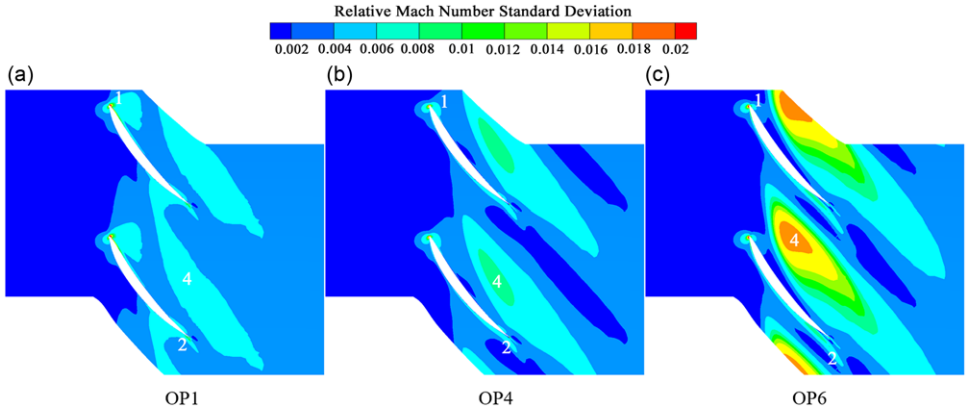

Figure 17. *Distributions of relative Mach number standard deviation at the 95% span.*

6.0 Conclusion

Blade geometrical deviations significantly influence the compressor performance. Relevant numerical calculations are performed to investigate the influence of the geometric uncertainty on the performance and determine the critical geometric variables. The uncertainty quantitative and sensitivity analyses give the following conclusions:

1. Blade geometric deviations cause the average compressor performance to be lower than the designed value, and the fluctuation ranges of the total pressure ratio and isentropic efficiency decrease for lower mass flow rates. The blade geometrical deviations significantly influence the flow field structure in the blade root and tip regions, and the influence on the blade root (tip) region decreases (increases) for lower flow rates.
2. In high flow conditions, the compressor total pressure ratio is most sensitive to the stagger angle and suction surface thickness deviations. At lower flow rates, the sensitivity of the compressor total pressure ratio to the pressure surface thickness deviation gradually increases, and the sensitivity to the stagger angle and suction surface thickness deviations gradually decreases.
3. The compressor isentropic efficiency has the greatest sensitivity to the suction surface thickness deviations in high flow conditions. However, at lower flow rates, the sensitivity of the compressor isentropic efficiency to the suction surface thickness and stagger angle deviations gradually decreases. The sensitivity of the compressor isentropic efficiency to the chord length and tip clearance deviations gradually increases, and these two deviations have the greatest influence on the compressor isentropic efficiency in low flow conditions.
4. The effects of various blade geometric deviations on the compressor performance are independent and linearly superimposed, and the combined effects of different geometric deviations are small. The impact of various geometric deviations on compressor performance varies under different operating conditions. When determining the tolerance band for blade machining, the tolerance band of geometric parameters that affects the main performance indicators of the compressor should be reduced appropriately. To reduce manufacturing costs, the tolerance band of geometric parameters that have less impact on compressor performance can be relaxed appropriately.

Acknowledgments. The authors thank for the supports by National Science and Technology Major Project J2019-I-0011. The authors also would like to acknowledge the supports by The Innovation Foundation for Doctor Dissertation of Northwestern Polytechnical University CX2024061.

Competing interests. The authors declare that they have no competing interests.

References

[1] An, G., Kang, J., Zou, Y., Zhang, L., Lang, J., Yuan, W. and Zhang, Q. Investigation of the unsteady flow in a transonic axial compressor adopted in the compressed air energy storage system, *J. Energy Storage*, 2023, **63**, p 106918.

[2] An, G., Kang, J., Wang, L., Zhang, L., Lang, J. and Li, H. Decoupling and reconstruction analysis in a transonic axial compressor using the dynamic mode decomposition method, *Phys. Fluids*, 2023, **35**, (8), p 084120.

[3] Zhang, L., Kang, J., Lang, J., An, G. and Zhang, Q. Stall evolution mechanism of a centrifugal compressor with a wide-long vaneless diffuser, *J. Therm. Sci.*, 2024, **33**, pp 899–913.

[4] Spieler, S., Staudacher, S., Fiola, R., Sahm, P. and Weißschuh, M. Probabilistic engine performance scatter and deterioration modeling, *J. Eng. Gas Turb. Power*, 2008, **130**, (4), pp 042507.

[5] Dow, E.A. and Wang, Q. The implications of tolerance optimization on compressor blade design, *J. Turbomach.*, 2015, **137**, (10), p 101008.

[6] Wang, J. and Zheng, X. Review of geometric uncertainty quantification in gas turbines, *J. Eng. Gas Turb. Power*, 2020, **142**, (7), p 070801.

[7] Bammert, K. and Sandstede, H. Influences of manufacturing tolerances and surface roughness of blades on the performance of turbines, *J. Eng. Power*, 1976, **98**, (1), pp 29–36.

[8] Lange, A., Voigt, M., Vogeler, K., Schrapp, H., Johann, E. and Gümmer, V. Probabilistic CFD simulation of a high-pressure compressor stage taking manufacturing variability into account, American Society of Mechanical Engineers, ASME Turbo Expo 2010: Power for Land, Sea, and Air, 14–18 June 2010, Glasgow, UK. GT2010-22484.

[9] Lange, A., Voigt, M., Vogeler, K., Schrapp, H., Johann, E. and Gümmer, V. Impact of manufacturing variability and nonaxisymmetry on high-pressure compressor stage performance, *J. Eng. Gas Turb. Power*, 2012, **134**, (3), p 032504.

[10] Lange, A., Voigt, M., Vogeler, K., Schrapp, H., Johann, E. and Gümmer, V. Impact of manufacturing variability on multistage high-pressure compressor performance, *J. Eng. Gas Turb. Power*, 2012, **134**, (11), p 112601.

[11] Goodhand, M.N. and Miller, R.M. The impact of real geometries on three-dimensional separations in compressors, *J. Turbomach.*, 2012, **134**, (2), p 021007.

[12] Goodhand, M.N., Miller, R.M. and Lung, H.W. The impact of geometric variation on compressor two-dimensional incidence range, *J. Turbomach.*, 2014, **137**, (2), p 021007.

[13] Cheng, C., Wu, B., Zheng, H. and Gao, L. Effect of blade machining errors on compressor performance, *Acta Aeronaut. Astronaut. Sin.*, 2020, **41**, (2), pp 28–38. [in Chinese]

[14] Dow, E.A. and Wang, Q. Simultaneous robust design and tolerancing of compressor blades, American Society of Mechanical Engineers, ASME Turbo Expo 2014: Turbine Technical Conference and Exposition, 16–20 June 2014, Düsseldorf, Germany. GT2014-25795.

[15] Lamb, C.T. and David, L.D. Performance-based geometric tolerancing of compressor blades, American Society of Mechanical Engineers, ASME Turbo Expo 2004: Power for Land, Sea, and Air, 14–17 June 2004, Vienna, Austria. GT2004-53592.

[16] Garzon, V.E. and David, L.D. Impact of geometric variability on axial compressor performance, *J. Turbomach.*, 2003, **125**, (4), pp 692–703.

[17] Jonas, M., Gantner, S., Städing, J. and Friedrichs, J. A machine learning based approach of performance estimation for high-pressure compressor airfoils, American Society of Mechanical Engineers, ASME Turbo Expo 2018: Turbomachinery Technical Conference and Exposition, 11–15 June 2018, Oslo, Norway. GT2018-75372.

[18] Marcello, A., Spinella, S. and Rinaudo, S. Stochastic response surface method and tolerance analysis in microelectronics, *COMPEL*, 2003, **22**, (2), pp 314–327.

[19] Brahmachary, S., Fujio, C., Aksay, M. and Ogawa, H. Design optimization and off-design performance analysis of axisymmetric scramjet intakes for ascent flight, *Phys. Fluids*, 2022, **34**, (3), p 036109.

[20] Maria M.C., Ahlfeld, R., Rosic, B. and Montomoli, F. Uncertainty quantification of leakages in a multistage simulation and comparison with experiments, *J. Fluid. Eng.*, 2018, **140**, (2), p 021110.

[21] Shi, W., Chen, P., Li, X., Jing, R. and Jiang, H. Uncertainty quantification of the effects of squealer tip geometry deviation on aerothermal performance, *P. I. Mech. Eng. A-J Pow.*, 2020, **234**, (7), pp 1026–1038.

[22] Guo, Z. and Chu, W. Stochastic aerodynamic analysis for compressor blades with manufacturing variability based on a mathematical dimensionality reduction method, *P. I. Mech. Eng. C-J Mec.*, 2022, **236**, (10), pp 5719–5735.

[23] Guo, Z., Chu, W. and Zhang, H. Uncertainty analysis of global and local performance impact of inflow and geometric uncertainties using sparse grid-based non-intrusive polynomial chaos, *P. I. Mech. Eng. A-J Pow.*, 2022, **236**, (7), pp 1239–1256.

[24] Chu, W., Ji, T., Chen, X. and Luo, B. Mechanism analysis and uncertainty quantification of blade thickness deviation on rotor performance, *P. I. Mech. Eng. A-J Pow.*, 2023, **237**, (6), pp 1188–1202.

[25] Ji, T., Chu, W., Liang, C. and Meng, D. Uncertainty quantification on the influence of blade thickness deviation at different rotational speeds based on flow dissipation analysis, *Phys. Fluids*, 2023, **35**, (6), p 066126.

[26] Wang, W., Chu, W., Zhang, H. and Kuang, H. Experimental and numerical study of tip injection in a subsonic axial flow compressor, *Chinese J. Aeronaut.*, 2017, **30**, pp 907–917.

[27] Chi, Z., Chu, W., Zhang, Z. and Zhang, H. Research on the stability enhancement mechanism of multi-parameter interaction of casing treatment in an axial compressor rotor, *P. I. Mech. Eng. G-J Aer.*, 2022, **236**, (12), pp 2405–2419.

[28] Chi, Z., Chu, W., Zhang, H., and Zhang, Z. Stall margin evaluation and data mining based multiobjective optimization design of casing treatment for an axial compressor rotor, *Phys. Fluids*, 2023, **35**, (8), p 086117.
[29] Zhang, H., Liu, W., Wang, E., Wu, Y. and Yao, W. Mechanism investigation of enhancing the stability of an axial flow rotor by blade angle slots, *P. I. Mech. Eng. G-J Aer.*, 2019, **233**, (13), pp 4750–4764.
[30] Denton, J.D. Some limitations of turbomachinery CFD, American Society of Mechanical Engineers, ASME Turbo Expo 2010: Power for Land, Sea, and Air, 14–18 June 2010, Glasgow, UK. GT2010-44021.
[31] Luo, J. and Liu, F. Statistical evaluation of performance impact of manufacturing variability by an adjoint method, *Aerosp. Sci. Technol.*, 2018, **77**, (7), pp 471–484.
[32] Debusschere, B.J., Najm, H.N., Matta, A., Knio, O.M., Ghanem, R.G. and Le Maı;tre, O.P. Protein labeling reactions in electrochemical microchannel flow: Numerical simulation and uncertainty propagation, *Phys. Fluids*, 2003, **15**, (8), pp 2238–2250.
[33] Chen, H., Wang, Q., Hu, R. and Constantine, P. Conditional sampling and experiment design for quantifying manufacturing error of transonic airfoil, American Institute of Aeronautics and Astronautics, 49th AIAA Aerospace Sciences Meeting including the New Horizons Forum and Aerospace Exposition, 4–7 January 2011, Orlando, Florida. AIAA 2011-658.
[34] Babacan, S.D., Molina, R. and Katsaggelos, A.K. Bayesian compressive sensing using laplace priors, *IEEE T. Image Process.*, 2010, **19**, (1), pp 53–63.
[35] Blatman, G. and Sudret, B. An adaptive algorithm to build up sparse polynomial chaos expansions for stochastic finite element analysis, *Probabilist. Eng. Mech.*, 2010, **25**, (2), pp 183–197.
[36] Sobol, I.M. Global sensitivity indices for nonlinear mathematical models and their Monte Carlo estimates, *Math. Comput. Simulat.*, 2001, **55**, (1), pp 271–280.
[37] Kang, Y.E., Yang, S. and Yee, K. Physics-aware reduced-order modeling of transonic flow via β-variational autoencoder, *Phys. Fluids*, 2022, **34**, (7), pp 076103.
[38] Guo, Z., Chu, W. and Zhang, H. A data-driven non-intrusive polynomial chaos for performance impact of high subsonic compressor cascades with stagger angle and profile errors, *Aerosp. Sci. Technol.*, 2022, **129**, p 107802.
[39] Sarabia Aldana, C.A., Medina-Torres, L., Calderas, F., Ramírez-Torres, L.A., Núñez-Ramírez, D.M., Herrera-Valencia, E.E., Bernad-Bernad M.J. & Manero, O. Hemorheological and biochemical study in patients with liver cirrhosis, *Phys. Fluids*, 2022, **34**, (4), p 041907.

Cite this article: Ji T.Y., Chu W.L. and Guo Z.T. Uncertainty quantification and sensitivity analysis of blade geometric deviation on compressor performance. *The Aeronautical Journal*, https://doi.org/10.1017/aer.2024.65